Apoptosis (2014) 19:1301–1316
DOI 10.1007/s10495-014-1018-8

ORIGINAL PAPER

Apoptotic agents inducing genotoxicity-specific chromatin changes

Gaspar Banfalvi

Published online: 15 July 2014

Abstract To visualize characteristic chromatin distortions we have distinguished first among regularly occurring intermediates of chromatin structures in mammalian (Indian muntjac, CHO, murine preB, rat liver, rat myeloid leukemia, K562 human erythroid leukemia) and *Drosophila* nuclei. Fluorescence microscopy of chromatin structures isolated from nuclei of reversibly permeable cells revealed a common pathway of chromatin condensation in mammalian cells. Different intermediates in mammalian and *Drosophila* cells indicate alternative mechanisms of chromosome condensation. Genotoxic agents such as irradiation (alpha, gamma, UV-B) and heavy metals (Cd, Pb, Ni, Hg, Ag) caused alterations in chromatin structures leading to apoptosis. Injury-specific chromatin changes manifested at significantly lower concentrations than non-specific signs of cellular toxicity, suggesting that preapoptotic events are useful indicators of genotoxicity.

Keywords Interphase chromatin · Chromosome condensation · Indicators of apoptosis · Genotoxic agents · Apoptotic chromatin changes

Introduction

Apoptotic signals and pathways

There are different groups of apoptosis inducing signals including: chemicals (e.g. antibiotics, ionophores, chemotherapeutic agents, heavy metals, free radicals, glucocorticoids, methylating agents, antiviral, anticancer agents, cytokines, alkaloids, etc.), physical insults (radiation, heat shock), viruses (Sindbis, Baculo, HIV-1), cells (cytotoxic T cells), cytokines (TNFα, TNFß), absence or loss of trophic factors (glucose, hormones, growth factors), other factors (p53, c-myc, CED-2,3,4, CED9 mutations, Fas/Apo-1, IL-1ß converting enzyme), etc. Based on external and internal stimuli, apoptosis can be categorized and divided in two principal pathways known as extrinsic pathway activated by the ligation of death signals to their receptors (Fig. 1a) and intrinsic pathway emerging from mitochondrial stress (Fig. 1b).

Once apoptotic signals reach the nucleus and/or the mitochondria, chromatin degradation ensues, apoptosis becomes irreversible. Apoptosis was originally described as morphological changes, among them chromatin condensation being the most recognizable nuclear hallmark of apoptosis. One would assume that some of the apoptotic chromatin changes reflect the type of genotoxic agent. To test the validity of this hypothesis we have used different apoptotic agents, among them heavy metals and irradiations. The aim of this review is to summarize characteristic structural changes in chromatin upon genotoxic treatment and to compare these alterations to those intermediates that are involved in the common pathway of chromosome condensation of healthy eukaryotic cells. Specific chromatin changes generated by different genotoxic agents have not been reviewed so far. This review focuses on early stages of characteristic morphological chromatin alterations causing apoptosis. Less attention will be paid to DNA fragmentation and other biochemical aspects of genotoxicity.

G. Banfalvi (✉)
Department of Microbial Biotechnology and Cell Biology, University of Debrecen, 1 Egyetem Square, Debrecen 4010, Hungary
e-mail: bgaspar@unideb.hu

Chromatin damages during apoptosis

Generally known chromatin changes follow cellular distortions including rounding up of cells, detachment

from the monolayer in cell cultures, blebbing, shrinkage and undergoing a so called apoptotic dance [2]. Alternatively, early cellular changes are preceeded by chromatin condensation, formation of crescent-shaped masses, aggregation and the disappearance of nucleoli [3]. Chromatin condensation itself has been divided in two distinct parallel pathways: (a) early chromatin compaction leading to large-scale DNA fragmentation and peripheral chromatin condensation and (b) late chromatin changes involving Apaf-1 and caspases, as well as CAD, mitochondrial endoG and nuclear DNase I resulting in oligosomal and final DNA fragmentation [4].

Methods to detect apoptosis

Detection of apoptotic cells, monitoring their progression to cell death, developing strategies that regulate apoptotic pathways, became an essential task of basic research. Various methods have been employed to detect apoptosis including direct measurement of apoptotic cells with flow cytometry and in situ labeling, as well as RNA, DNA, and protein assays that are indicative of apoptotic molecules.

Protocols for apoptosis and kits are available as:

Cytotoxic assays

- Radioactive and non-radioactive assays that measure the permeability of plasma membrane.
- Colorimetric assays based on the reductive capacity of mitochondria.

General methods

- Staining of apoptotic cells.
- Fluorescence activated cell sorting (FACS).
- DNA fragmentation (DNA laddering analysis).
- TdT-mediated dUTP Nick-End Labeling (TUNEL) analyis.
- *In situ* end labeling (ISEL).
- Annexin-V analysis, measuring alterations in plasma membranes.
- Detection of apoptosis related proteins (Western Blotting, binding assays).
- Caspase immunoassays for apoptosis detection.

Alternative methods to detect apoptosis

Less frequently known and used methods detect apoptosis based on:

(a) Light scattering flow cytometry.
(b) Automated imaging of cell surface area.
(c) Apoptotic chromatin changes.

Light scattering flow cytometry

Light scattering instruments, especially flow cytometers can be easily adapted for measurements of apoptosis to estimate cellular DNA degradation during programmed cell death. The analysis is related to particle size and amplifies the apoptotic signal and shows more convincingly the reduction in the cell size of apoptotic cells [5]. The DNA content in itself is an important indicator of apoptotic cells accumulating at the sub-G_1/G_0 window in the flow cytometric profile. This signal is normally too low to be detected in healthy cells. In damaged cells the amplification of small apoptotic signals by forward scatter analysis allows a more detailed analysis and provides quantified data. An example of forward scatter analysis after γ-irradiation of K562 cells is given in Fig. 2. The number of apoptotic cells after γ-irradiation is seen in the sub-G_1 marker window increasing from 4.8 to 15.6 % within 1 day. Apoptosis inducing treatment causes the temporal accumulation of apoptotic cells, the increase of cells in G_1/G_0 and in G_2/M and the decrease of S phase cells (Fig. 2).

Automated imaging of cell surface area

This test distinguishes between apoptosis and necrosis based on the shrinkage or expansion of cells. We have established a time-lapse video microscopy system to follow the movement of single cells for a longer period of time up to 1 week. The system was used originally to describe the movement of normal cells and cells subjected to cell death, then applied for the automated imaging of visible cell surface. The surface area of a monolayer healthy cell is much larger than its detached round form. Cell surface changes under normal cell growth show the visible surface of a detached, round HaCaT cell (Fig. 3A/a) being smaller than its round, divided daughter cells (Fig. 3A/b). The moderate movement of cell division is indicated by the zig–zag line (Fig. 3A/c). Separated daughter cells regain their original size before they return to the monolayer and start a new cycle (Fig. 3A/d).

Apoptosis-inducing treatment generates rapid rhythmical contraction of membrane blebbing referred to as “dance of death” [2, 6]. The cell death of a monolayer HaCaT cell subjected to apoptotic treatment is shown in the graphic presentation characteristic of apoptosis (Fig. 3B). After 1 μM $Pb(NO_3)_2$ apoptotic treatment (Fig. 3B/a) the visible surface of the detached, shrunken and quickly moving cell was drastically reduced (Fig. 3B/b). Blebbing under vigorous movement (“dance macabre”) contributed to a temporary increase of cell surface (Fig. 3B/c) followed by the complete disintegration and lysis of the apoptotic cell (Fig. 3B/d).

The cell surface analysis after necrosis-inducing treatment (50 μM $Pb(NO_3)_2$ showed four distinguishable stages

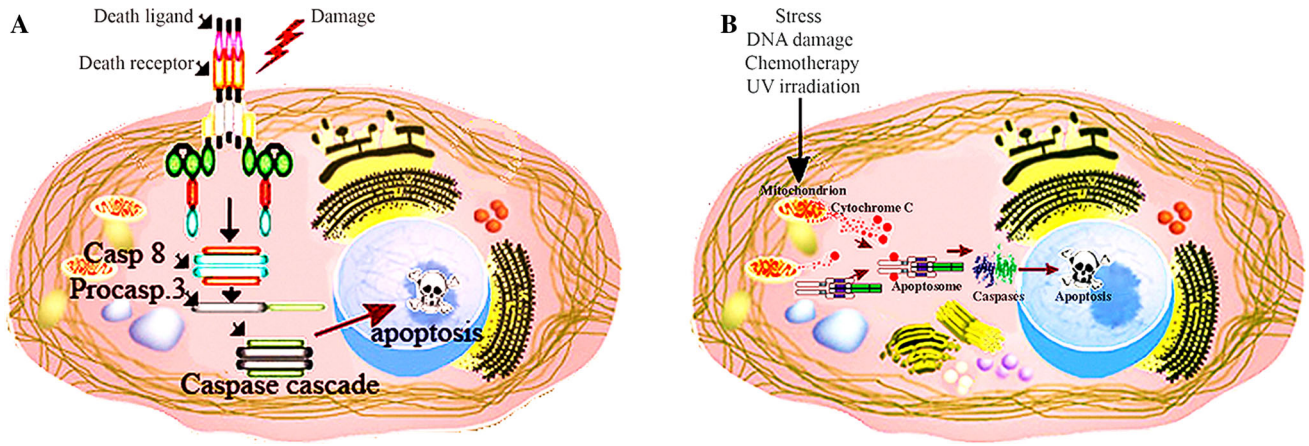

Fig. 1 General pathways of apoptosis. **a** *Extrinsic* apoptosis: death ligands bind to the death receptors resulting in the clustering of death receptor proteins followed by the induction of initiator then executioner caspases leading to the destruction of nuclear material and cell death without mitochondrial involvement. **b** *Intrinsic* mitochondrial pathway of apoptosis caused by external damaging agents (radiation, chemotherapy) and internal stress (e.g. reactive oxygen species). Cytochrome c released from mitochondria binds to cytosolic Apaf-1 protein and ATP to form apoptosomes that attract and activate procaspase 9 and coupled to the *extrinsic* downstream pathway through the executioner caspases. With permission [Ref. [1], Figs. 4.10. p.226 and 4.15. p. 244]

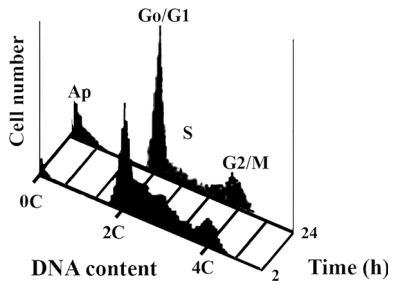

Fig. 2 Apoptosis detected by forward scattering of light. Equal number (5×10^5) of K562 cells were exposed to 4 Gy γ-irradiation using a ^{60}Co source at a dose rate of 0.9 Gy/min. One aliquote was incubated for 2 h, the other for 24 h at 37 °C then stained with propidium iodide and subjected to forward light scatter analysis. The C-values of major peaks are indicated. Ap, apoptotic cells. With permission [Ref. [5], Fig. 2D]

of cell death (Fig. 3C). The monolayer surface of the necrotic cell (Fig. 3C/a) rounded up and the visible surface became about 3–4 time larger (Fig. 3C/b). Further ($\sim 8 \times$) increase of cell surface (Fig. 3C/c) was followed by a moderate decrease in cell surface after cellular disruption (Fig. 3C/d), in conformity with the general observation of necrotic enlargement and disruption of cells.

Intermediates of chromosome condensation

As far as the mechanism of supranucleosomal chromosome condensation is concerned, there is no general agreement among scientists. The debate is indicated by different models of mitotic chromosome formation including the radial loop [8, 9], successive hierarchical folding, combined radial loop/helical folding [10, 11] and axial glue mechanisms [12]. Less attention has been paid to interphase chromosomes and their large-scale structures that were deduced from higher order mitotic chromosome models rather than from microscopic images. The detection of genotoxic chromatin changes necessitates basic knowledge about structural forms of interphase chromosomes of healthy cells. The scarcity of morphological evidence regarding the intermediates of chromatin folding has several reasons:

Lack of methods to open nuclear membrane When metaphase chromosomes are isolated by standard fixation using methanol-acetic acid, only two types of microscopic structures are visible: (a) the closed nuclear membrane prevents the look behind the nuclear curtain and we see only interphase nuclei (Fig. 4a), or the nuclear membrane disappears completely and metaphase chromosomes become visible (Fig. 4b). To overcome the permeability barrier that prevents the opening of nuclei we have adapted reversible permeabilization, which allows the visualization of several new interphase chromosomal structures [13]. These structural forms seen in Fig. 4c–f obviously represent a lower compaction than metaphase chromosomes, but belong to the pattern of interphase chromosome condensation. One could argue that methanol-acetic acid fixation of chromosomes operating by dehydration is damaging the 3D architecture of chromatin structures, causing flattened nucleus and damaged chromosome morphology [14, 15]. However, then the metaphase chromosome structure should also be doubted as it has been isolated by the same procedure as other intermediates of chromatin condensation. During reversible permeabilization we have shortened the pulse of slightly hypotonic buffer treatment from 10 to 1 min in the presence of dextran, which prevents the

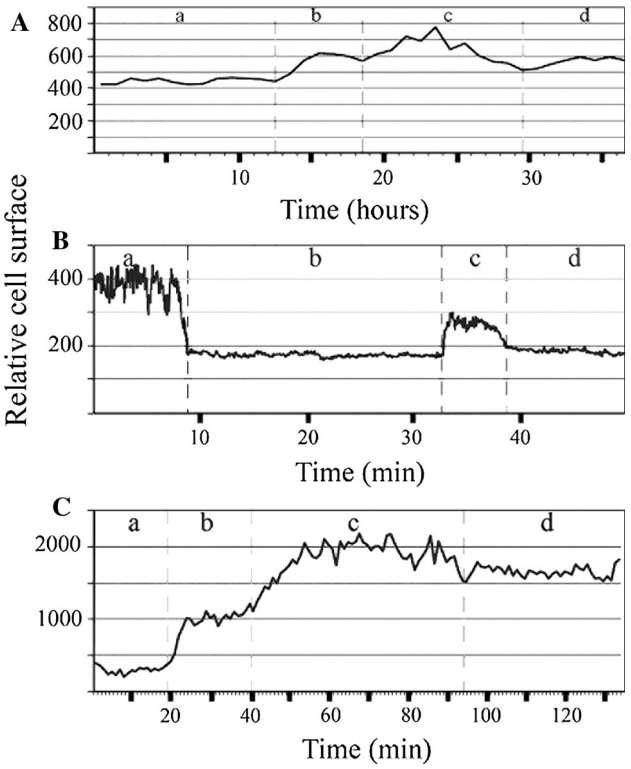

Fig. 3 Characteristic cell surface changes during cell division measured by time-lapse imaging. **A** Changes in the visible cell surface during the cell division of a control HaCaT cell. *a* Relative surface of a visible monolayer cell, *b* the visible surface of the detached round shaped daughter cells, *c* surface of the daughter cells after they return to the monolayer, *d* new cell division of an emerging round cell. **B** Temporal profile of apoptotic development after 1 μM $Pb(NO_3)_2$ treatment showing characteristic surface changes. *a* monolayer cell, *b* detachment and apoptotic shrinkage, *c* complete disintegration, *d* lysis. **C** Temporal stages of necrotic cell surface increase after 50 μM $Pb(NO_3)_2$ treatment: *a* monolayer cell, *b* beginning of necrosis *c* further necrotic enlargement, *d* dead cell. With permission [Ref. [7], Figs. 3, 6, 8]

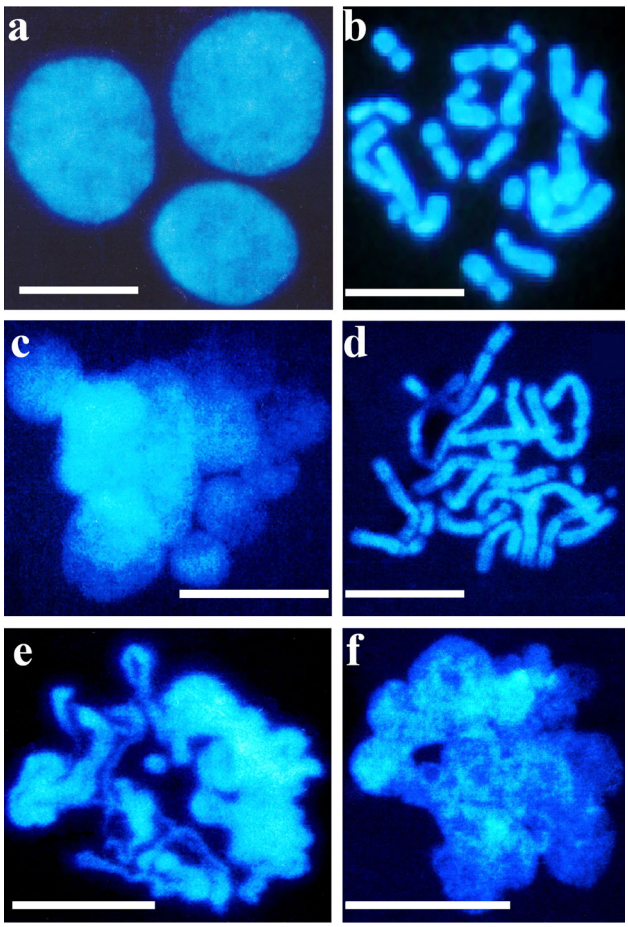

Fig. 4 Isolation of interphase chromosomes from nuclei of CHO cells. Chromatin structures of normal cells: **a** nuclei, **b** metaphase chromosomes. Intermediates of chromatin condensation after reversible permeabilization of CHO cells **c–f** isolated from nuclei by the same method. *Bars*, 5 μm each. Photography: G. Banfalvi, 1988

disruption of cells and maintains their viability [16]. Nuclei of permeable cells open freely without sticking together when they are placed back in high (10 %) fetal bovine serum containing medium. Others have found that a more drastic and longer double hypotonic treatment for permeabilization was not critical for cell viability [15].

Different patterns of chromosome condensation Chromosomes are not condensed to the same compaction in different species. Known examples are the lampbrush chromosomes [17], which represent a special form of chromosomes found in the oocytes of immature eggs of most animals with the notable exception of mammals. Another example is the giant polytene chromosome [18] commonly occurring in the secretory tissues of many dipterans such as the salivary glands of *Drosophila melanogaster* or the Malpighian tubules of *Drosophila* and other insects, or in other structures in protists, plants, and mammals.

We have found that in *Drosophila* cells the chromosomes consists of smaller units named rodlets. The fluorescent images of these rodlets were subjected to computer-aided visualization. The chromatin fibers around the rodlets turned out to consist of plectonemic loops of 12–15 nucleosomes corresponding to an average length of 300 nm. Theoretical considerations led to a plectonemic model of chromatin condensation explaining the 30 nm chromatin fibers that were further condensed to the 300 nm loop structure (Fig. 5A) (reviewed by [19]).

The supranucleosomal chromatin organization of *Drosophila* resembles that of the mammalian chromosomes. The notable difference is that in mammalian cells the rodlets are replaced by longer spiral units of higher flexibility. These thick chromatin coils turn around the nuclear scaffold, favoring the helical coil mechanism of chromosome formation (Fig. 5B).

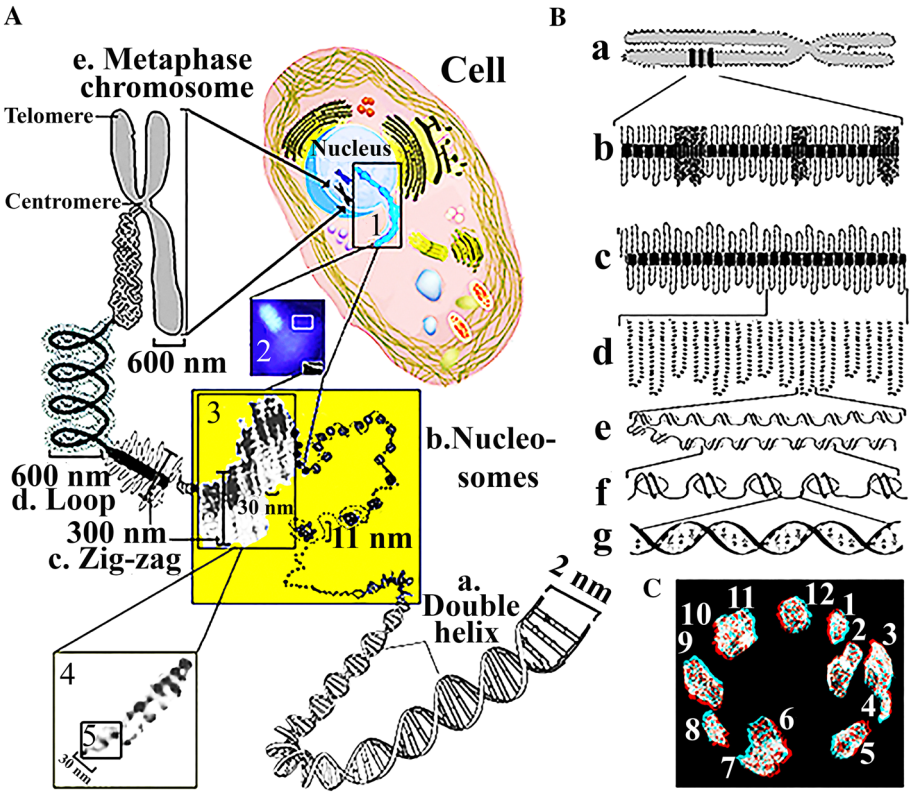

Fig. 5 Alternative mechanisms of chromosome condensation. **A** Plectonemic chromatin condensation in *Drosophila* cells. From upper right to lower left direction: *1* Chromosomes slipping out of the nucleus from the permeable cell. *2* Smaller chromosomal unit (rodlet). *3 Boxed area* of 2 converted to black-and-white negative image, subjected to computer image analysis (300 nm loop structure). *4* "Beads on string" forming a hairpin structure (30 nm structure). *5 Boxed area* in 4 showing the nucleosomal arrangement (11 nm structure). From lower right to upper left direction: *a* double-stranded DNA (diameter 2 nm), *b* nucleosomes (11 nm), *c* plectonemic nucleosomal arrangement (30 nm fiber), zig–zag loops of plectonemic fibers (300 nm), *d* forming axial rodlets (600 nm), *e* metaphase chromosome. With permission (Ref. [19], Fig. 5). **B** Helical-coiling model of chromosome condensation in rat myeloid leukemia cells. *a* Two chromatids of metaphase chromosome (diameter 1,400 nm). *b* Heterogeneous distribution of chromatin loops forming chromatid bands corresponding to the spiral units (700 nm). *c* Helical coiling of loops around the nonhistone protein core (700 nm). *d* Chromatin loops (300 nm). *e* Plectonemic folding of"beads on string" bringing about chromatin fibrils (30 nm). *f* Nucleosome"beads on string" (11 nm). *g* Double helical DNA (2 nm). With permission [Ref. [20], Fig. 5]. **C** Anaglyph-transmission electronmicroscopy visualization of the 12 haploid chromosomes in the type B spermatogonium of the garden snail. Transmission electron microscopic images of the numbered (1–12) *Helix lucorum* chromosomes made by T. Roszer and G. Nagy. TESLA BS 540 transmission electron microscope was used in digital processing mode (dTEM)

We have assumed that chromosomes in animals of lower complexity, but of similar nuclear size are less condensed. This idea was tested in *Helix lucorum* (garden snail) by visualizing the chromosomes of type B spermatogonia through transmission electronmicroscopy. Similar to the spermatogonia in the human testis [21], the nuclei of *H. lucorum* are larger than in other cells. The electron microscopy of chromosomes of garden snail spermatogonium was supported by anaglyph 3D visualization achieved by means of filters of different (red and cyan) colors (Fig. 5C). Anaglyph 3D imaging helped to distinguish between overlapping chromosomes. The relatively round shape and wide diameter of chromosomes of the gastropod garden snail are in conformity with the notion that the compaction of chromosomes may be related not only to the length of DNA, but also to the availability of the nuclear space. The economy of chromosome folding was evidenced during the trivision of hyperploid cells that was preceeded by the triploidization of the nuclear material seen as a three-pointed star corresponding to the most optimal configuration in which the three angles are 120° [22]. The data of others also indicate that steric constraints determine structure, rather than innate chromosome architecture or function-driven anchoring, with interphase chromatin organization governed primarily by opposition between needs for de-condensation and the space available [23].

Technical difficulties to visualize large scale chromatin structures These limitations included: (a) low spatial resolution of light microscopy, (b) nonspecific staining of DNA, (c) the difficulty of visualizing 3-D structures even in thin sections of cells by electron microscopy, (d) the

stickiness of the nuclear material and (e) the sensitivity of chromatin conformation to even small environmental (e.g. ionic) changes. Improved visualization of chromatin folding patterns within diploid nuclei and polytene chromosomes was obtained using nonionic detergents in polyamine or divalent cation buffers to remove nucleoplasmic background staining [24]. This improvement allowed the visualization of individual chromatin fibers within a chromosome puff in polytene chromosomes. For diploid nuclei, the Belmont laboratory has chosen osmotic conditions that preserve in vitro the chromosome morphology [25]. This approach revealed large-scale chromatin fibers, termed chromonema fibers appearing as short fiber segments or more continuous fiber lengths, roughly 100 nm in diameter. Others reported that imaging techniques failed to show decondensed interphase chromosomal forms and little solid information was gained concerning the architecture of interphase chromosomes [26]. Studies that have used fluorescent in situ hybridization (FISH) technique proved to be damaging. As it has not been possible to visualize individual chromosomes of interphase cells, where chromosomes spend over 90 % of their time, photoactivation of labeled histone 3 was applied to observe interphase structures [23]. Bioimaging by green fluorescent protein was also expected to improve the visualization of individual proteins in single cells [27]. Time-lapse video microscopy was introduced to see morphological changes in single cells of cell cultures [28–32]. Cell growth could be traced by video microscopy over longer periods of time, on the order of days [28, 33]. However, cell death caused by genotoxic damage often may last longer [29] than time-lapse cinemicroscopy could follow. Moreover, extended observations through fluorescence microscopy are likely to result in significant light energy exposure and cellular damage [34]. Due to these damaging effects we have used neither photoactivation nor green fluorescein proteins during time-lapse bioimaging experiments.

To overcome the technical difficulties we use reversibly permeabilized cells that allow us: (i) to open the nucleus in the interphase, (ii) to isolate intermediates of chromatin condensation, (iii) to observe individual chromosome structures by fluorescence microscopy, (iv) to analyze the temporal order of early chromosomal forms in a cell cycle-dependent manner in synchronized cells and (v) to test specific changes in chromatin structure caused by genotoxic agents.

Common intermediates of chromatin condensation

By reversing permeabilization, it was possible to confirm the existence of a flexible chromatin folding pattern through a series of transient geometric forms such as supercoiled, circular forms, chromatin bodies, thin and thick fibers and elongated chromosomes [35]. Earlier results showed that the incorporation of biotin-11-dUTP interfered with chromatin condensation, leading to the accumulation of early intermediates of chromatin condensation being in decondensed state [13]. To study the temporal order of chromatin condensation the incorporation of nucleotides was omitted and subpopulations of cells were synchronized by counterflow centrifugal elutriation [36, 37]. After the reversal of permeabilization chromatin structures of four different types of mammalian cells (Indian muntjac, CHO, murine pre-B, human K-562) were isolated from their synchronized fractions and visualized by fluorescence microscopy. In all four cell types decondensed veil-like structures were observed in early S phase (between 2.0 and 2.25 C-value), supercoiled chromatin later in early S (2.25–2.5 C), fibrous structures in early mid S phase (2.5–2.75 C), ribboned structures before mid S (2.75–3.0 C), chromatin bodies in mid S phase (3.0–3.25 C), continuous chromatin strings later in mid S phase (3.25–3.5), elongated pre chromosomes in late S phase (3.5–3.75 C), precondensed chromosomes at the end and after S phase (2.75–4.0 C) [38] (Fig. 6). Fluorescence microscopy revealed that interphase chromosomes are similar in different mammalian cells reflecting a common mechanism of condensation. Chromosomes are not separate entities but form a linear array arranged in a semicircle (Fractions 5 and 6 in Fig. 6). Linear arrangement was confirmed by computer image analysis.

Cellular toxicity of heavy metals

Early observations of studies related to the cellular toxicity of heavy metals were reported back in 1936. These experiments have shown that primarily the cellular membranes were affected by heavy metals causing the loss of potassium from rabbit erythrocytes [39, 40] in the order of $Pb^{2+} > Au^{+} > Hg^{2+}$ [41]. Passow and Rothstein [42] found that Hg^{2+} treatment led to the complete loss of K^{+} and that the mercury induced loss of K^{+} from yeast cells was an all-or-none effect. Cu^{2+} also caused loss of K^{+} from baker's yeast, but similar concentration of Pb^{2+} or Zn^{2+} did not have any effect, but might have affected the uptake of glucose, the inhibition of metabolic activities (respiration and glycolysis) and the block of cell division [42]. $HgCl_2$ disrupted primarily the plasma membrane, whereas the primary effect of $CdCl_2$ was exerted on cell proliferation [43]. It was found that potassium, which has normally a low permeability, was released due to increasing concentration of bound copper. The increase of permeability of cells was considered to be the primary toxic effect of copper. Potassium-depleted cells remained viable

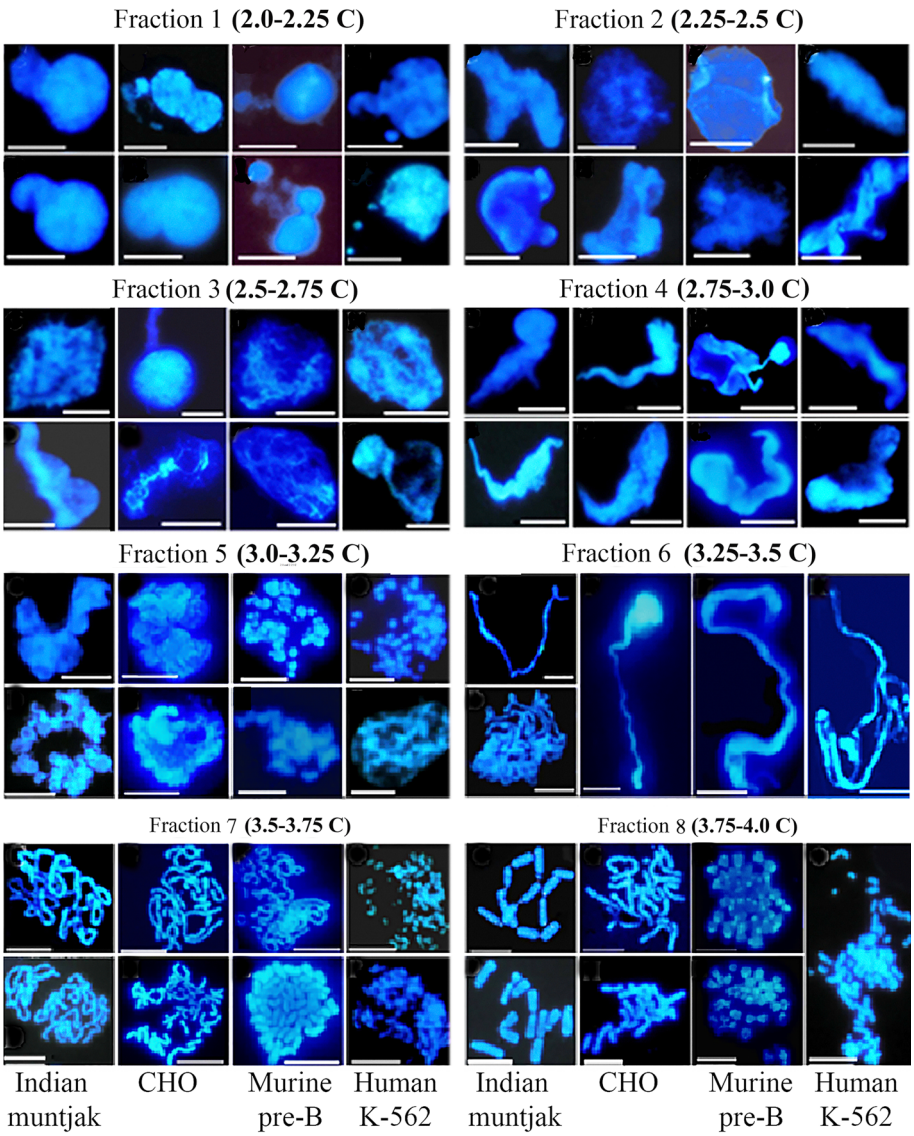

Fig. 6 Common pathway of chromosome condensation. Interphase chromosome structures isolated from synchronized fractions of mammalian cells (Indian muntjac, CHO, murine pre-B, human K-562). The upper and lower figures in each pair show the same or similar intermediates of chromosome condensation. *Bars*, 5 μm each. Modified with permission [Ref. [38], Figs. 1 and 2]

if subsequently transferred to a copper-free medium [44]. As this experiment can be regarded as one of the early attempts to reversibly permeabilize cells, the importance of reversible permeabilization under possibly mildest conditions is pointed out. Reversible permeabilization was a prerequisite for breaking the barrier of cellular membranes by using dextran T-150 in a slightly hypotonic buffer to introduce nucleotides [16]. This hypotonic treatment is a modified method of Halldorson et al. [45]. The importance of dextran in the permeabilization is underlined since it is a macromolecule that does not enter the cell membrane, but as a surface coat prevents hypotonic cell disruption and maintains the viability of cells [46]. Others have used permeable cells to incorporate oligonucleotides into cells [47, 48].

In animal cells the rapid interaction of mercury or copper with the membrane could be followed by the penetration into the interior of the muscle cell [49]. Another function associated with the interior of the cell is cellular respiration. It is likely that in different animal cells a similar sequence of events occurs. Some of the effects on membrane function include: changes in the permeability to glycerol produced by copper [50] and by mercury [51]; losses of K^+ from red blood cells produced also by lead, mercury, gold, and silver [41]; inhibition of surface-bound invertase in the yeast cell by silver and mercury [52]. Mercury, cadmium, lead and thallium are known to poison glucose metabolism in cells. Heavy metals may also induce oxidative stress and produce reactive oxygen species causing different types of DNA damages. Structural changes involve nucleotide bases, cross-links, strand breaks, formation of bulky DNA-adducts, etc. Here we discuss only the chromatin toxicity of a selected group of heavy metals including cadmium, lead, mercury, uranium, zinc and silver.

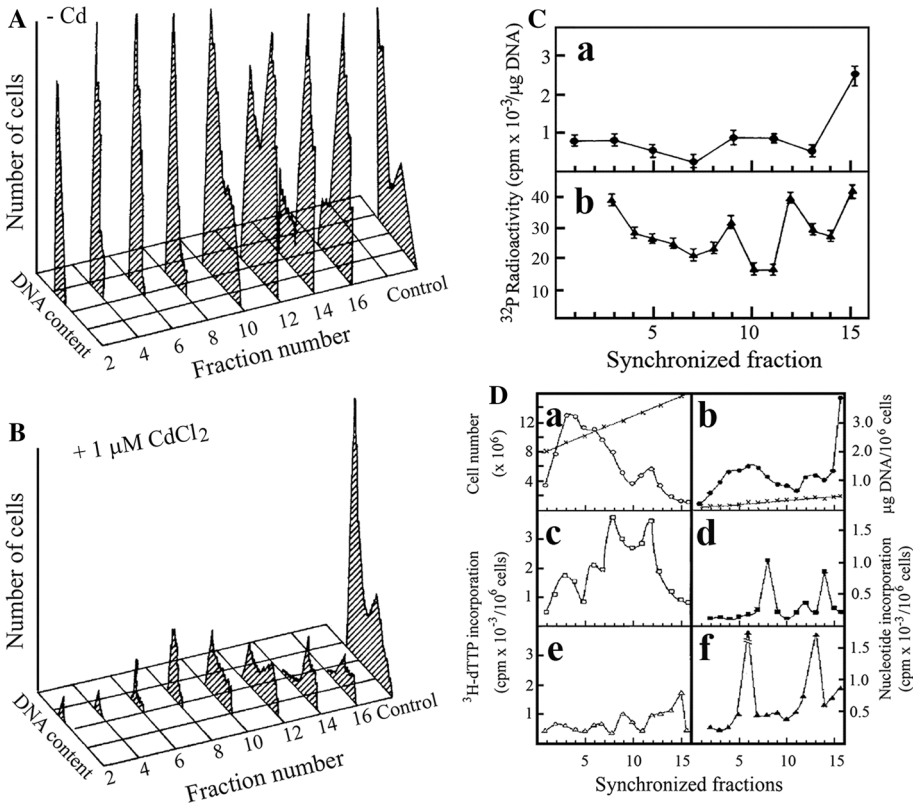

Fig. 7 Cd induced cellular changes in CHO cells. **A** Flow cytometry of control cells synchronized by centrifugal elutriation. **B** Flow cytometric profiles of cells treated with $CdCl_2$ (1 μM) for 15 h. **C** Strand breaks in control cells (C/a) and in $CdCl_2$ (1 μM) treated cells (C/b). **D** Elutriation profiles of replicative and repair DNA synthesis in control and $CdCl_2$ (0.5 μM) treated cells. The change in the rate of replicative and repair synthesis was followed throughout the S phase in synchronized populations of CHO cells. Cell number in elutriated fractions of control cells (o-o) and DNA content (x-x) of control cells (D/a). Cell number in Cd-treated cells (•–•) and DNA content (x-x) of $CdCl_2$ treated cells (D/b). Replication profile of control (D/c) and Cd treated (D/d) cells. Repair synthesis in control (D/e) and Cd treated (D/f) cells. With permission [Ref. [53], Figs. 1–3 combined]

Cd induced cellular changes

Low concentration (1 μM) $CdCl_2$ treatment reduced cell growth (Fig. 7A, B), generated DNA strand breaks (Fig. 7C/a, b), affected the amount of isolable DNA (Fig. 7D/a, b), reduced replicative DNA synthesis (Fig. 7D/c, d), increased repair DNA synthesis (Fig. 7D/e, f) in a cell cycle-dependent manner, when 16 synchronized fractions were collected.

Cd induced chromatin changes

Cadmium treatment caused characteristic chromatin damages in CHO cells: (a) the absence of decodensed veil-like structures and premature chromatin condensation in the form of apoptotic chromatin bodies in early S phase, (b) the absence of fibrous structures, lack of supercoiled chromatin, the appearance of uncoiled ribboned chromatin and perichromatin bodies in early mid S phase, (c) the presence of perichromatin fibrils and chromatin bodies in mid S, (d) early intra-nuclear inclusions, elongated forms of premature chromosomes later in mid S, (e) the exclusion of chromatin bodies and large-sized perichromatin granules in late S [54]. Here only the most characteristic changes caused by Cd(II) are shown in CHO cells as large extensive disruptions and holes in the nuclear membrane and stickiness of incompletely folded chromosomes [54] (Fig. 8A, elutriation fractions 4, 6 and 8).

Cadmium induced chromatin changes seen in murine preB cells [55] and in K562 cells [56] (bottom left panels, Fig. 8A) corresponded to those in CHO cells after Cd treatment indicating that these chromatin changes independent of the cell type are genotoxicity specific. Chromatin changes characteristic to cadmium treatment were seen in different mammalian cells [54–56] as severe disruptions of the nuclear membrane observed from the mid S phase till the end of S phase, and in G2 and M phases. These disruptions did not allow further distinction among the final stages of chromatin condensation, resulting in nuclei with big holes and sticky, imperfectly condensed chromosomes.

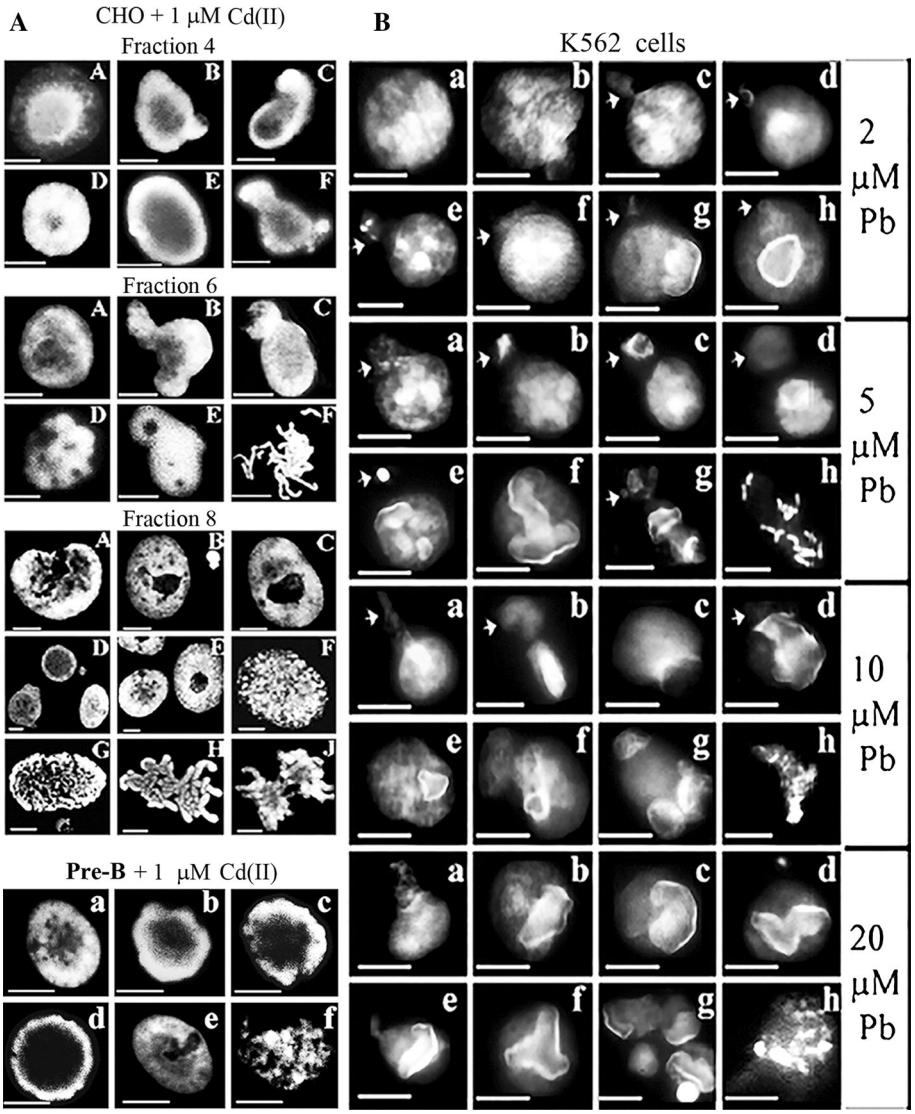

Fig. 8 Cd and Pb induced chromatin changes. CHO or murine preB cells were treated with 1 μM $CdCl_2$ for 15 h. **A** CHO cells were synchronized by centrifugal elutriation and 8 fractions were collected. Typical chromatin structures in elutriation fractions 4, 6 and 8 are to be compared to Fig. 6 as control. Chromatin structures of preB cells after Cd treatment correspond to those seen in CHO cells. **B** K562 cells were treated with different concentrations of $Pb(NO_3)_2$ for 15 h. Isolation of chromatin structures and fluorescence microscopy were carried out after DAPI staining. *Bars* 5 μm each. Control chromatin structures for genotoxic treatments are shown in figure 6. With permissions [Ref. [54], parts of Figs. 9–11] and [Ref. [56], Figs. 3 and 4]

Chromatin toxicity of $Pb(NO_3)_2$

At low (2–20 μM) Pb(II) concentrations the extrusion of polarized chromatin resembled that of micronucleus formation in K-562 cells (Fig. 8B). The lack of supercoiling seems to prevent the formation of chromatin bodies, which are regarded as the earliest visible forms of interphase chromosomes. A typical feature was the early condensation of chromatin bringing about lobular chromatin ribbons arranged in a semicircular manner (Fig. 8B at 2 μM). Beside chromatin ribbons, large chromatin clusters were formed after 5 μM $Pb(NO_3)_2$ treatment. Bent lobular chromatin ribbons dominated the pictures at higher (10–20 μM $Pb(NO_3)_2$) concentrations (Fig. 8B, lower panels). Characteristic distortions allowed a clear distinction between Cd and Pb toxicity at micromolar concentrations. The visualization of these chromatin changes is relatively easy and fast harboring the potential of early differential diagnostics between Cd and Pb poisoning from a relatively small populations of cells. Chromatin alterations in K562 cells upon Pb treatment [56] can be summarized as:

(a) Chromatin changes were dose dependent with higher frequency at elevated Pb(II) concentrations.
(b) The absence of chromatin loops and chromatin bodies is accounted for by the prevention of supercoiling.
(c) Decondensed and improperly folded chromatin is excluded from the nucleus, resembling micronucleus formation seen in Fig. 8B: at 2 μM Pb(II) in panel g, at 5 μM in panel d, at 20 μM in panel a.
(d) The most characteristic features of Pb toxicity are highly condensed lobular ribbons arranged in a semicircular manner.
(e) Pb treatment caused the clustering of chromatin in five major groups. In rat liver nuclei six major chromatin domains were seen [57].

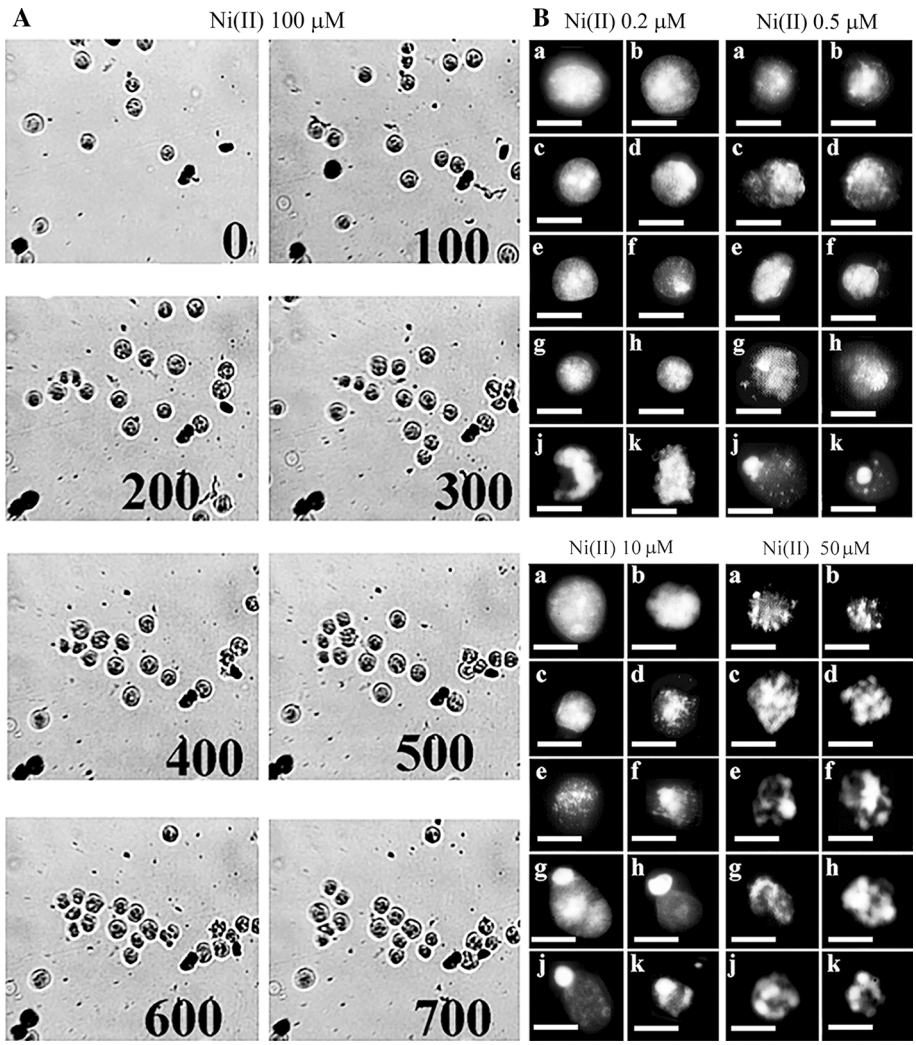

Fig. 9 Cellular and chromatin changes induced at different concentrations of $Ni(Cl)_2$. A. K562 cells were grown in 25 ml T-flasks and treated with 100 μM $Ni(Cl)_2$, placed on inverted microscope sitting in a carbon dioxide incubator. Photographs were taken every minute by custom built video camera attached to the microscope and connected to the computer. The motion of individual cells is indicated by their changing position. Black numbers indicate the time of photography in minutes after heavy metal treatment. B. K562 cell were treated with different concentrations of Ni(II), then subjected to reversible permeabilization and isolation of chromatin structures. Fluorescence microscopy was performed after staining with DAPI. *Bars*, 5 μm each. With permission [Ref. [62], Figs. 7.3, 7.5 and 7.6]

(f) Low concentrations of lead nitrate (2–20 μM) had no effect on the viability of HL-60 cells, only higher (30–150 μM) caused apoptosis [58]. In in vivo experiments only a high dose of 1 mmol/kg $Pb(NO_3)_2$ caused the enlargement of apoptotic bodies of liver cells [59]. Rat adrenal medulla also showed resistance towards high concentration (100 μM) of lead nitrate [60]. Moderately high (40 μM) $Pb(NO_3)_2$ concentration was necessary to trigger apoptosis in rat hepatic stem cells [61]. Beside the variable sensitivity of different strains the toxicity of Pb(II) may depend on the density of the cell culture. High cell culture density is likely to reduce the cytotoxicity of Pb. The higher protein concentration of the nucleus relative to the cytoplasm could explain the higher frequency of interaction of Pb(II) with nuclear proteins and its correspondingly higher chromatin toxicity and detection at as low as 2–10 μM Pb(II) concentrations. The significant differences underline the diagnostic importance of chromatin distortions relative to the measurement of cellular toxicity.

Cellular toxicity of Ni(II)

Apoptotic effect exerted by heavy metals (Cd^{2+} Hg^{2+} and Pb^{2+}) on the chromatin structure and described in CHO, murine preB and K562 cells [54, 56, 63] are adversely affecting gene structure and function. These xenobiotic heavy metals are likely to initiate carcinogenesis [64]. The size of K562 cells varied only slightly upon treatment within a wide range (0.2–100 μM) of $NiCl_2$ concentration. The movement of individual cells was visualized by time-lapse video microscopy under physiological and Ni(II) induced genotoxic conditions. Cellular toxicity of Ni(II) was seen as vigorous cellular motion monitored at relatively high 100 μM Ni(II) concentration by time-lapse microscopy (Fig. 9A). Although the Ni-treated cells moved faster than control cells, this motion was less intense than the so called "apoptotic dance" observed after Pb-treatment of HaCaT cells, and resulted in sticky and clumping together cells.

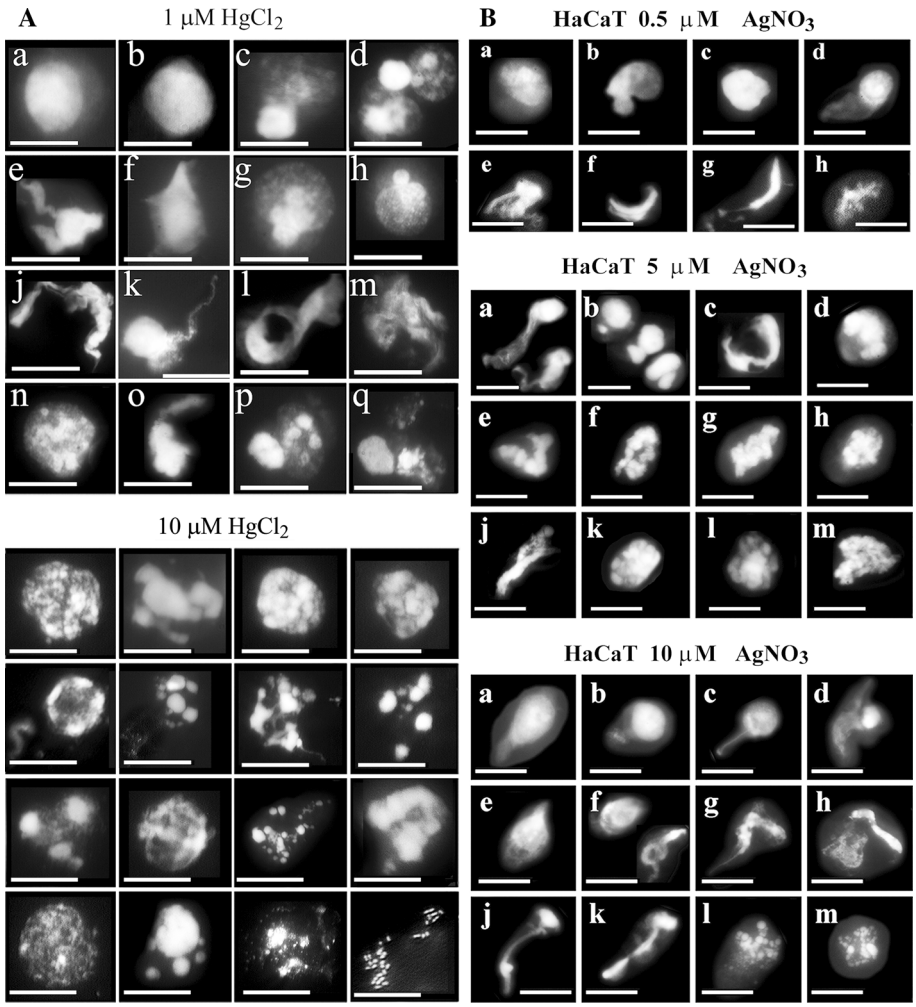

Fig. 10 Chromatin changes induced at different concentration of $Hg(Cl)_2$ and $AgNO_3$. After heavy metal treatment K562 cells were subjected to reversible permeabilization, isolation of chromatin structures. Fluorescence microscopy was performed after staining with DAPI. **A** Chromatin structures after Hg(II) treatment. With permission [Ref. [63], Fig. 3 and 4]. B. $AgNO_3$ treatment. With permission [Ref. [65], Fig. 9.6 and 9.7]. *Bars*, 5 μm each

Chromatin toxicity of $NiCl_2$

To the best of our knowledge large-scale chromatin changes induced by Ni(II) have not been studied earlier. Low (0.2–0.5 μM) concentrations of Ni(II) caused the polarization and the rejection of apoptotic bodies (Fig. 9B upper panels). The polarization of nuclear material turned to premature condensation at 10 μM Ni(II), the rest of the chromatin remaining in highly decondensed fibrillary stage. The concentration dependent polarization and premature local heterochromatization were the most characteristic signs of chromatin toxicity of Ni(II). Necrotic changes took place at ≥50 μM $NiCl_2$ with less fibrillary chromatin, moderately increased and round shaped nuclei (Fig. 9B lower panels).

To summarize the Ni(II) induced chromatin changes: (a) one of the most important functions, the cellular movement is moderately impaired, (b) the nuclear effect, namely heterochromatization, is dominating the picture after Ni(II) treatment, (c) the chromatotoxic effect is manifested as retarded condensation at different stages of the chromatin folding process, and (d) the multiple forms of chromatin structures retarded by Ni(II) depend on the concentration of the heavy metal and the duration of incubation.

Cellular and chromatin changes caused by $HgCl_2$

Time lapse video photography was used to follow the movement of individual cells after in vitro treatment with $HgCl_2$. Cellular changes caused by mercuric ions were characterized by their properties of causing reduced cellular motility (10–50 μM), and complete lack of cellular movement at higher concentrations (100–1000 μM). Results showed that micromolar concentrations of Hg(II) that did not cause noticeable alterations in the cellular morphology of K562 cells, but initiated chromatin changes as earliest signs of cytotoxicity. Major types of distortions in the nuclear material were highly condensed supercoiled and decondensed veil-like chromatin, decondensed chromosomes rejected as clustered puffs and often the nuclear material was broken down to apoptotic bodies (Fig. 10A

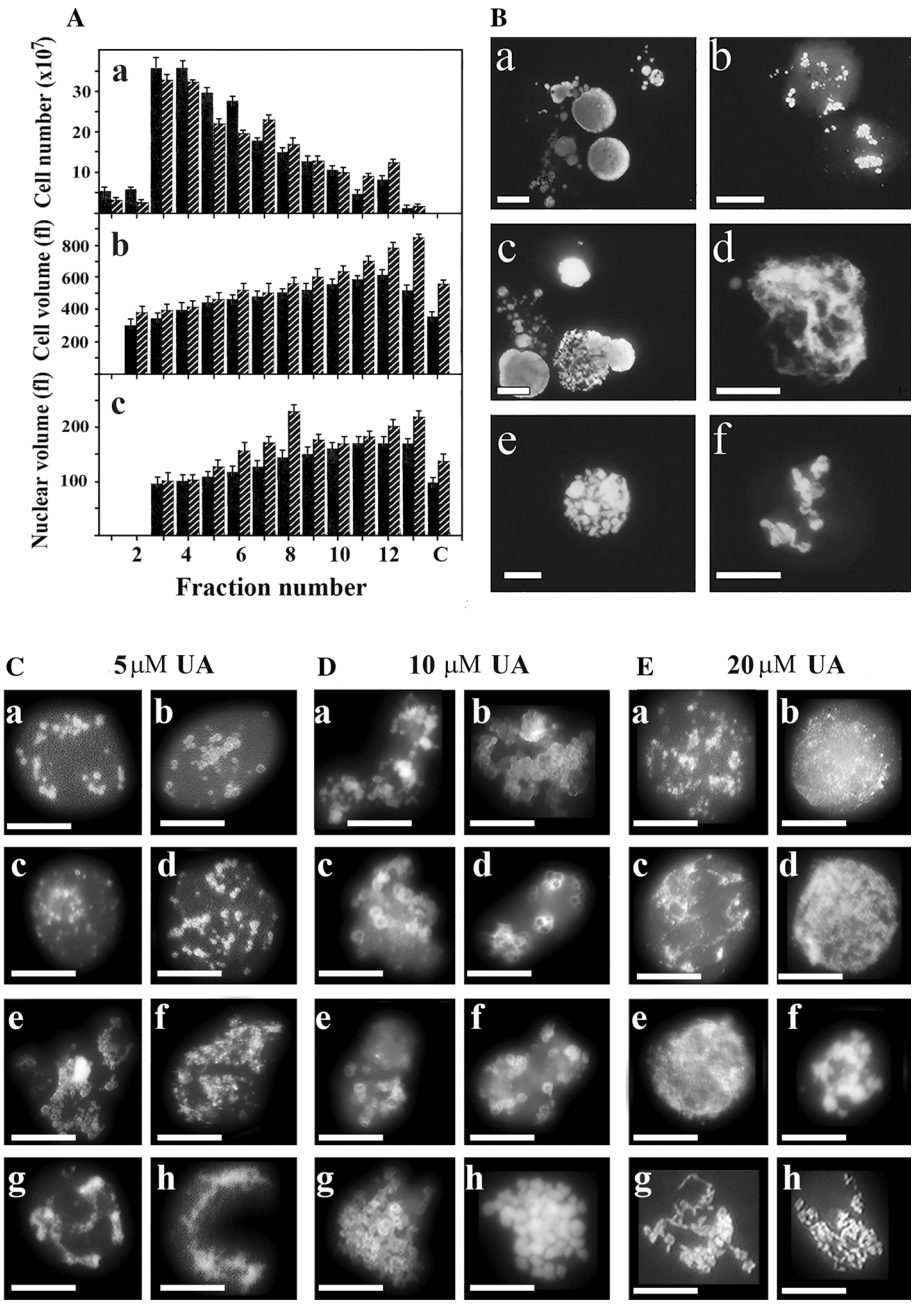

Fig. 11 Characteristic chromatin changes caused by γ irradiation and alpha emitting uranyl acetate. **A** The effect of γ-irradiation on cell number *a*, cell volume *b*, and nuclear volume *c* in elutriated fractions. *Black columns* indicate non-irradiated cells, *striped columns* correspond to values obtained from irradiated cells. **B** Intermediates of chromatin condensation in preB 70Z/3 cells γ-irradiated with 400 R, incubated for 2 h and synchronized by centrifugal elutriation and collecting 9 fractions. Chromatin structures were isolated and visualized after DAPI staining. Apoptotic bodies in nuclei from fractions 4, 5 and 6, corresponding to panels a, b and c, respectively. Fibrous chromatin (fraction 7, d). Incomplete transition from fibrous chromatin to precondensed chromosomes (fractions 8 and 9; e and f, respectively). With permission (Ref. [66] Figs. 3 and 5). The effect of alpha radiation on chromatin structure at low (5 μM) uranyl acetate (**C**) at higher UA concentration (10 μM) (**D**), and at high (20 μM) UA concentration (**E**). *Bars* 5 μm each)

upper panels). Nuclear changes caused by Hg(II) acetate at 10 μM were characterized by apoptosis seen as broken nuclei and apoptotic bodies (Fig. 10A lower panels). High concentration of Hg^{2+} ions (100 μM) initiated necrotic nuclear changes, with enlarged leaky or opened nuclei (not shown).

Apoptotic chromatin changes caused by Ag ions

Fluorescence microscopic visualization of large-scale chromatin structures took place in HaCaT and K562 cells. These experiments revealed that after $AgNO_3$ treatment at low concentrations, that were regarded earlier as subtoxic levels (<1 μM), chromatin changes were noticeable early signs of cytotoxicity with K562 cells. Typical nuclear changes induced by silver nitrate involved the polarization of precondensed and the extrusion of decondensed chromatin seen as chromatin tailing. The tail ("comet") formation seen with HaCaT cells was dependent on silver nitrate concentration (Fig. 10B). Elevated silver nitrate concentrations (10–15 μM) caused nuclear shrinkage with infrequent formation of apoptotic bodies. Higher Ag^{+}

concentrations (20–50 μM) allowed the expansion of the nuclear material without necrotic disruptions (not shown). The chromatin tail formation could be accounted for by the decreased chromatin supercoiling and could be related to a dose dependent reduction of ATP content, cell viability and increased production of reactive oxygen species.

Effect of ionizing irradiation on chromatin structure

Alterations in chromatin structure generated by gamma irradiation

Apoptotic changes were visualized in a cell cycle dependent manner at the chromatin level by fluorescence microscopy in non-irradiated murine preB cells and after 400 rad Co^{60} irradiation. Fluorescence microscopy of chromatin structures belonging to the interphase of the cell cycle confirmed the existence of specific geometric forms in nuclei of non-irradiated cells (Fig. 6 serving as control). Our results have shown that relative to the control upon γ-irradiation (i) the cell growth was reduced (left panels, Fig. 11A/a), (ii) the cellular and nuclear sizes were increased (left panels, Fig. 11A/b and c), (iii) the DNA content was lower in each elutriated subpopulation of cells. The progression of the cell cycle was arrested in the early S phase at ~2.4 C value, the chromatin condensation was blocked between the fibrillar chromatin and precondensed elongated chromosomal forms [66] and (iv) the number and size of apoptotic bodies after "γ bombardment" were inversely correlated with the progression of the cell cycle, with many small apoptotic bodies in early S phase and less and larger apoptotic bodies in late S phase (left panels, Fig. 11B/a–f).

Chromatin changes in the presence of low concentration (5 μM) of uranyl acetate (UA)

Uranyl acetate (UA) is a water-soluble uranium compound often used as a stain in electron microscopy. The estimated toxic dose of UA in DMEM culture medium after 48 h incubation of LLC-PK I cells was (1 mM) [67]. Due to the relatively high radiation resistance of K562 cells against gamma irradiation [5] and shorter time of incubation (15 h) we have applied higher doses (5, 10 and 20 μM) of UA. At already lower dose (5 μM) UA caused characteristic chromatin changes seen as small round, often circular bodies resembling chromatin bodies (Fig. 11C/a–d), and the appearance of chromatin ribbons containing dots corresponding to apoptotic bodies (Fig. 11C/e–h).

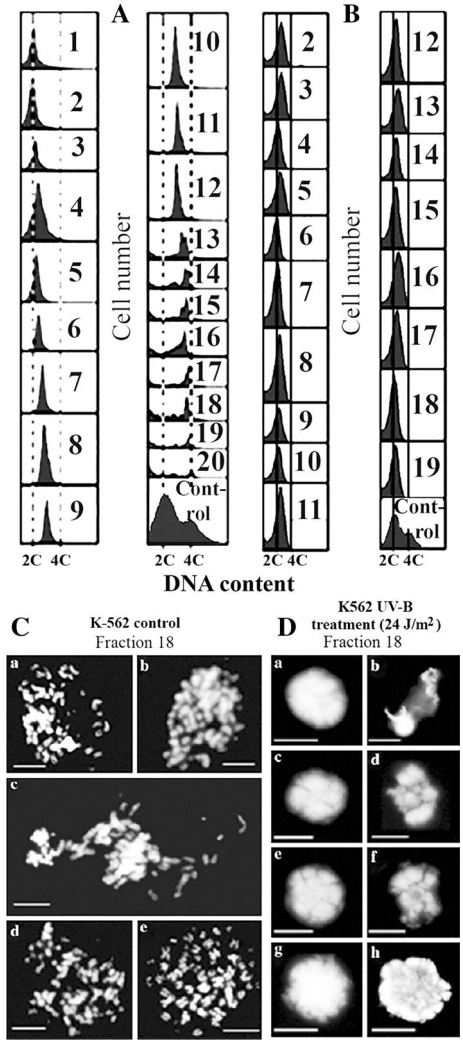

Fig. 12 Characterization of UV-B irradiated cell populations. Cells were synchronized and 20 fractions were collected by centrifugal elutriation. K562 cells were UV irradiated with 24 J/m^2. **A** Cell cycle patterns of non irradiated cells. **B** Irradiated K562 cells analyzed by FACS after propidium iodide staining. **C** Complete chromosome formation in non-irradiated cells. **D** Segregation of nuclear material in irradiated cells. Chromatin structures isolated from cells of irradiated cells (fraction 18) covered by chromatin fibrils did not reach the metaphase stage. *Bars*, 5 μM each. With permission ([68], Figs. 2 and 5)

Chromatin changes at higher concentration (10 μM) of uranyl acetate

The chromatin distontions resembled those observed at lower UA concentration, with the notable exception that fewer and larger apoptotic bodies were formed and covered by a fine fibrillary network (Fig. 11D/a–h).

Chromatin changes at high (20 μM) uranyl acetate concentration

Incoherent large chromatin associations containing many small apoptotic dots or circles dominated the pictures

(Fig. 11E/a–f). Sticky chromosomes did not reach the metaphase (Fig. 11E/g–h).

Changes in chromatin structure after non-ionizing UV irradiation

The flow cytometric profiles of the 20 fractions of non-irradiated K562 cells were used to estimate their DNA content (Fig. 12A, upper left panels) ranging between 2.07 and 3.88 C-values. The separation of UV-B irradiated cells (24 J/m^2) was carried out in the same manner, but their C-values remained between 2.2 and 2.4 C-values corresponding to the fibrillary chromatin structure (Fig. 12B, upper right panels).

At lower doses of UV light (6, 12 J/m^2) chromatin changes occurred only occasionally. Higher UV light dose (24 J/m^2) manifested as an increased fibrillary cloud covering and blurring the condensing chromatin structures. Occasionally small apoptotic bodies were seen, but contrary to gamma irradiation [66] they were not characteristic of UV irradiation. Neither chromatin bodies, nor completely folded chromosomal forms could be observed. Relative to control metaphase chromosomes (Fig. 12C, lower left panels), primitive, early forms of chromatin condensation were covered with a faint chromatin halo that did not reach the stage of metaphase (Fig. 12D, lower right panels). The fine fibrillary network dominated the pictures without progression of supercoiling that would lead to compact structures [68]. The early block of chromatin condensation at its fibrillary stage probably plays an important role in direct photoreactivation and nucleotide excision repair of pyrimidine dimers and 6,4 photoproducts.

Conclusion

Chromatin condensation in mammalian cells

Reversibly permeabilized cells have been used to visualize interphase chromatin structures after DAPI staining by fluorescence microscopy. In healthy mammalian cells decondensed veil-like structures were observed in early S-phase, supercoiled chromatin later in the early S, fibrous structures in early mid S, ribboned chromatin in mid-S, continuous chromatin strings in late mid-S phase, elongated pre chromosomes in late S phase, precondensed chromosomes at the end and after S phase. Neither interphase, nor metaphase chromosomes are separate entities, but form a linear array arranged in a semicircle. The temporal pattern of chromatin condensation was compared in mammalian (Indian muntjac, CHO, murine preB and human K562 erythroleukemia) cells in a cell cycle dependent manner. Fluorescence microscopy showed that regular and temporally distinct chromatin structures follow a general pathway of chromatin condensation in mammalian cells [35, 38]. Enlarged nuclei of rat myelocytic leukemia cells revealed further intermediates of chromatin condensation not seen previously, including spiral units that are involved in the chromonemic folding of metaphase chromosomes. The existence of spiral subunits favors the helical coil model of chromosome condensation [20].

Chromatin condensation in Drosophila cells

The compaction of *Drosophila* chromosomes did not reach that of mammalian cells in the final stage of condensation. *Drosophila* chromosomes consist of smaller rodlets that are not apoptotic bodies. These small and relatively rigid units of chromosomes could correspond to the more flexible spiral subunits of mammalian cells. The review demonstrated that the nucleosomal chromatin ("beads on string") does not form a solenoid structure, rather the topological arrangement consists of meandering and plectonemic loops. The zig–zag array of fibers consisting of 12–15 nucleotides with a length of 270–330 nm ($\approx$300 nm) showed decondensed extended strings, condensed loops and coiled condensed loops. Theoretical considerations led to the plectonemic model of chromatin condensation giving an explanation how the 30 nm chromatin fibers are formed and further condensed to the 300 nm chromatin loops in *Drosophila* cells [19]. Typical genotoxic chromatin alterations observed after various treatments were absent in non-treated cells excluding the possibility of artifact formation.

Alterations in chromatin structure after genotoxic treatment

Abnormal chromosomal forms were found after treatment of cells with heavy metals including cadmium, lead, nickel, mercury and silver and upon ionizing irradiation or non-ionizing UV-B. As apoptotic changes have not been characterized at the chromatin level in interphase, we have analyzed the structural effects of apoptosis induced under genotoxic conditions such as heavy metal treatment, emission of alpha particles by uranium acetate, gamma and ultraviolet irradiations. Besides revealing intermediates of the normal supranucleosomal organization of DNA it was shown that structural aberrations take place in chromatin organization upon genotoxic treatments. These changes are not uniform and may generate characteristic distortions in the intermediates of chromatin condensation that can be of differential diagnostic importance. Structural alterations suggest that some of these and probably other preapoptotic events can be recognized based on their injury-specific

chromatin changes. Apoptosis was originally described as a morphological process characterized by nuclear changes, disintegration of nucleolus and chromatin undergoing unusual generalized condensation. The cellular and nuclear condensation distinguished apoptosis from the swelling of necrotic cells. The cell death-related terminology includes now many other related processes such as autophagy, entosis, mitotic catastrophe, necrosis, necroptosis, pyroptosis, etc. While the notion is emphasized that not only multicellular organisms die in thousands of ways, but also individual cells, the review cautions that beside characteristic chromatin changes there are less specific genotoxic insults that can generate similar distortions in the chromatin structure.

Acknowledgments This work was supported by Hungarian Scientific Research Fund (OTKA grant) T42762 grant to G.B. Transmission electron microscopic images of *Helix lucorum* chromosomes made in 2005 and provided by former PhD students, T. Roszer and G. Nagy are gratefully acknowledged.

References

1. Banfalvi G (2009) Apoptotic chromatin changes. Springer, Dordrecht, Fig. 1.10 p. 17, Fig. 4
2. Bernard J, Malawista SE (1995) Remembrance of professor Marcel Bessis (1917–1994). Blood Cell Mol Dis 21:152–155
3. Kerr JFR (1971) Shrinkage necrosis: a distinct mode of cellular death. J Pathol 105:13–20
4. Susin SA, Daugas E, Ravagnan L, Samejima K, Zamzami N, Loeffler M, Costantini P, Ferri KF, Irinopoulou T, Prévost MC, Brothers G, Mak TW, Penninger J, Earnshaw WC, Kroemer G (2000) Two distinct pathways leading to nuclear apoptosis. J Exp Med 192:571–580
5. Banfalvi G, Klaisz M, Ujvarosi K, Trencsenyi G, Rozsa D, Nagy G (2007) Gamma irradiation induced apoptotic changes in the chromatin structure of human erythroleukemia K562 cells. Apoptosis 12:2271–2283
6. Humke EW (2000) Web Alert Apoptosis. Chem Biol 7(2):R48–R49
7. Nagy G, Pinter G, Kohut G, Adam A, Trencsenyi G, Hornok L, Banfalvi G (2010) Time-lapse analysis of cell death in mammalian and fungal cells. DNA Cell Biol 29:249–259
8. Paulson JR, Laemmli UK (1977) The structure of histone depleted chromosomes. Cell 12:817–828
9. Adolph KW (1980) Isolation and structural organization of human mitotic chromosomes. Chromosoma 76:23–33
10. Rattner JB, Lin CC (1985) Radial loops and helical coils coexist in metaphase chromosomes. Cell 42:291–296
11. Boy De La Tour E, Laemmli UK (1988) The metaphase scaffold is helically folded: sister chromatids have predominantly opposite helical handedness. Cell 55:937–944
12. Kireeva N, Lakonishok M, Kireev I, Hirano T, Belmont AS (2004) Visualization of early chromosomal condensation: a hierarchical folding, axial glue model of chromosome structure. J Cell Biol 166:775–785
13. Banfalvi G (1993) Fluorescent analysis of replication and intermediates of chromatin folding in nuclei of mammalian cells. In: Bach PH, Reynolds CH, Clark JM, Mottley J, Poole PL (eds) Biotechnology applications of microinjection, microscopic imaging, and fluorescence. Plenum Press, New York, pp 111–119
14. Hepperger C, Otten S, von Hase J, Dietzel S (2007) Preservation of large-scale chromatin structure in FISH experiments. Chromosoma 116:117–133
15. Kobliakova I, Zatsepina O, Stefanova V, Polyakov V, Kireev I (2005) The topology of early- and late-replicating chromatin in differentially decondensed chromosomes. Chromosome Res 13:169–181
16. Banfalvi G, Sooki-Toth A, Sarkar N, Csuzi S, Antoni F (1984) Nascent DNA chains synthesized in recersibly permeable cells of mouse thymocytes. Eur J Biochem 139:553–559
17. Flemming W (1882) Zellsubstanz, Kern- und Zelltheilung. Vogel, Leipzig
18. Balbiani EG (1881) Sur la structure du noyau des cellules salivaires chez les larves de *Chironomus*. Zool Anz 4(637–641):662–666
19. Banfalvi G (2008) Chromatin fiber structure and plectonemic model of chromosome condensation in *Drosophila* cells. DNA Cell Biol 27:65–70
20. Trencsenyi G, Nagy G, Bako F, Kertai P, Banfalvi G (2012) Incomplete chromatin condensation in enlarged rat myelocytic leukemia cells. DNA Cell Biol 31:470–478
21. Paniagua P, Nistal M, Amat P, Rodriguez MC, Alonso JR (1986) Quantitative differences between variants of a spermatogonia in man. J Reprod Fertil 77:669–673
22. Nagy G, Kiraly G, Turani M, Banfalvi G (2013) Cell trivision of hyperploid cells. DNA Cell Biol 32:676–684
23. Müller I, Boyle S, Singer RH, Bickmore WA, Chubb JR (2010) Stable morphology, but dynamic internal reorganisation, of interphase human chromosomes in living cells. PLoS One 13(5):e11560. doi:10.1371/journal.pone.0011560
24. Bjorkroth B, Ericsson C, Lamb MM, Danehol B (1988) Structure of the chromatin axis during transcription. Chromosoma 96:333–340
25. Belmont AS, Braunfeld MB, Sedat JW, Agard DA (1989) Large-scale chromatin structural domains within mitotic and interphase chromosomes *in vivo* and *in vitro*. Chromosoma 98:129–143
26. Lemke J, Claussen J, Michel S, Chudoba I, Mühlig P, Westermann M, Sperling K, Rubtsov N, Grummt UW, Ullmann P, Kromeyer-Hauschild K, Liehr T, Claussen U (2002) The DNA-based structure of human chromosome 5 in interphase. Am J Hum Genet 71:1051–1059
27. Lippincott-Schwartz J, Snapp E, Kenworthy A (2001) Studying protein dynamics in living cells. Nat Rev Mol Cell Biol 2:444–456
28. Pulkinnen JO, Joensuu LH, Martikainen P, Servomaa K, Grénman R (1996) Paclitaxel-induced apoptotic changes followed by time-lapse video microscopy in cell lines established from head and neck cancer. J Cancer Res Clin Oncol 122:214–218
29. Forrester HB, Albright N, Ling CC, Dewey WC (2000) Computerized video time-lapse analysis of apoptosis of REC:Myc cells X-irradiated in different phases of the cell cycle. Radiat Res 154:625–639
30. Hoepfner D, Brachat A, Philippsen P (2000) Time-lapse video microscopy analysis reveals astral microtubule detachment in the yeast spindle pole mutant cnm67. Mol Biol Cell 11:1197–1211
31. Lane JD, Allan VJ, Woodman PG (2005) Active relocation of chromatin and endoplasmic reticulum into blebs in late apoptotic cells. J Cell Sci 118:4059–4071
32. Rieger MA, Schroeder T (2008) Exploring hematopoiesis at single cell resolution. Cell Tissues Organs 188:139–149
33. Hinchcliffe EH (2005) Using long-term time-lapse imaging of mammalian cell cycle progression for laboratory instruction and analysis. Cell Biol Educ 4:284–290
34. Dixit R, Cyr R (2003) Cell damage and reactive oxygen species production induced by fluorescence microscopy: effect on mitosis and guidelines for non-invasive microscopy. Plant J 36:280–290
35. Gacsi M, Nagy G, Pinter G, Basnakian AG, Banfalvi G (2005) Condensation of interphase chromatin in nuclei of Chinese hamster ovary (CHO-K1) cells. DNA Cell Biol 24:43–53

36. Banfalvi G (2008) Cell cycle synchronization of animal cells and nuclei by centrifugal elutriation. Nat Protoc 3:663–673
37. Banfalvi G (2011) Synchronization of mammalian cells and nuclei by centrifugal elutriation. Methods Mol Biol 761:25–45
38. Banfalvi G, Nagy G, Gacsi M, Roszer T, Basnakian AG (2006) Common pathway of chromosome condensation in mammalian cells. DNA Cell Biol 25:295–301
39. Henriques V, Orskov SL (1936) Untersuchungen fiber die Schwankungen des Kationgehaltes der roten Blutkörperchen. Skand Arch Physiol 74:63–78
40. Davson H, Danielli JF (1938) Studies on the permeability of erythrocytes factors in cation permeability. Biochem J 32:991–1001
41. Joyce CRB, Moore H, Weatherall M (1954) The effects of lead, mercury, and gold on the potassium turnover of rabbit blood cells. Br J Pharmacol Chemother 9:463–470
42. Passow H, Rothstein A (1960) The binding of mercury by the yeast cell in relation to changes in permeability. J Gen Physiol 43:621–633
43. Braeckman B, Raes H, Van Hoye D (1997) Heavy-metal toxicity in an insect cell line. Effects of cadmium chloride, mercuric chloride and methylmercuric chloride on cell viability and proliferation in *Aedes albopictus* cells. Cell Biol Toxicol 13:389–397
44. McBrien DCH, Hassal KA (1965) The effect of toxic doses of copper upon respiration, photosynthesis and growth of *Chlorella vulgaris*. Physiol Plant 20:113–117
45. Halldorson H, Gray DA, Shall S (1978) Poly (ADP-ribose) polymerase activity in nucleotide permeable cells. FEBS Lett 85:349–359
46. Kucera R, Paulus H (1982) Studies on ribonucleoside-diphosphate reductase in permeable animal cells. II. Catalytic and regulatory properties of the enzyme in mouse L cells. Arch Biochem Biophys 214:114–123
47. Lesh RE, Somlyo AP, Owens GK, Somlyo AV (1995) Reversible permeabilization: a novel technique for the intracellular introduction of antisense oligodeoxynucleotides into intact smooth muscle. Circ Res 77:220–230
48. Kobayashi S, Kitazawa T, Somlyo AV, Somlyo AP (1989) Cytosolic heparin inhibits muscarinic and alpha-adrenergic Ca^{2+} release in smooth muscle. Physiological role of inositol 1,4,5-trisphosphate in pharmacomechanical coupling. J Biol Chem 264:17997–18004
49. Demis DJ, Rothstein A (1955) Relationship of the cell surface to metabolism. XII. Effect of mercury and copper on glucose uptake and respiration of rat diaphragm. Am J Physiol 180:566–574
50. Jacobs MH, Glassman HN, Parpart AK (1950) Hemolysis and zoological relationship. Comparative studies with four penetrating non-electrolytes. J Exp Zool 113(2):277–300
51. Wilbrandt W (1941) Die Wirkung von Schwermetallsalzen auf die Erythrocyten- permeabilität für Glycerin. Pflüg Arch Ges Physiol 244(5):637–643
52. Myrbäck K (1957) Inhibition of yeast invertase (saccharase) by metal ions. V. Inhibition by mercury compounds. Arkiv Kemi 11:471–479
53. Banfalvi G, Littlefield N, Hass B, Mikhailova M, Csuka I, Szepessy E, Chou WM (2000) Effect of cadmium on the relationship between replicative and repair DNA synthesis in synchronized cho cells. Eur J Biochem 267:6580–6585
54. Banfalvi G, Gacsi M, Nagy G, Kiss BZ, Basnakian AG (2005) Cadmium induced apoptotic changes in chromatin structure and subphases of nuclear growth during the cell cycle in CHO cells. Apoptosis 10:631–642
55. Banfalvi G, Ujvarosi K, Trencsenyi G, Somogyi C, Nagy G, Basnakian AG (2007) Cell culture density dependent toxicity and chromatin changes upon cadmium treatment in murine pre-B cells. Apoptosis 12:1219–1228
56. Banfalvi G, Sarvari A, Nagy G (2012) Chromatin changes induced by Pb and Cd in human cells. Toxicol In Vitro 26:1064–1071
57. Trencsenyi G, Kertai P, Somogyi C, Nagy G, Dombradi Z, Gacsi M, Banfalvi G (2007) Chemically induced carcinogenesis affecting chromatin structure in rat hepatocarcinoma cells. DNA Cell Biol 26:649–655
58. Yedjou CG, Milner JN, Howard CB, Tchounwou TB (2010) Basic apoptotic mechanisms of lead toxicity in human leukemia (HI-60) cells. Int J Environ Res Publ Health 7:2008–2017
59. Columbano A, Ledda-Columbano GM, Coni PP, Faa G, Liguori C, Santa Cruz G, Pani P (1985) Occurrence of cell death (apoptosis) during the involution of liver hyperplasia. Lab Investig 52:670–675
60. Xu J, Ji L-D, Xu L-H (2006) Lead-induced apoptosis on PC 12 cells: involvement of p53, Bcl-2 family and caspase-3. Toxicl Lett 166:160–167
61. Agarwal S, Roy S, Ray A, Mazumbder S, Bhattacharya S (2009) Arsenic trioxide and lead acetate induce apoptosis in adult rat stem cells. Cell Biol Toxicol 25:403–413
62. Nagy G, Laza D, Ujvarosi K, Banfalvi G (2011) Chromatin toxicity of Ni(II) ions in K562 erythroleukemia cells. In: Banfalvi G (ed) Cellular effects of heavy metals. Springer, New York, pp 163–178
63. Farkas E, Ujvarosi K, Nagy G, Posta J, Banfalvi G (2010) Apoptogenic and necrogenic effects of mercuric acetate on the chromatin structure of K562 human erythroleukemia cells. Toxicol In Vitro 24:267–275
64. Kasprzak KS, Sunderman FW Jr, Salnikow K (2003) Nickel carcinogenesis. Mutat Res 533:67–97
65. Nagy G, Turani M, Kovacs KE, Banfalvi G (2011) Chromatin changes upon silver nitrate treatment in human keratocyte HaCaT and K562 erythroleukemia cells. In: Banfalvi G (ed) Cellular effects of heavy metals. Springer, New York, pp 195–217
66. Nagy G, Gacsi M, Rehak M, Basnakian AG, Klaisz M, Banfalvi G (2004) Gamma irradiation-induced apoptosis in murine pre-B cells prevents the condensation of fibrillar chromatin in early S phase. Apoptosis 9:765–776
67. Furuya R, Kumagai H, Hishida A (1997) Acquired resistance to rechallenge injury with uranyl acetate in LLC-PK1 cells. J Lab Clin Med 129:347–355
68. Ujvarosi K, Hunyadi J, Nagy G, Pocsi I, Banfalvi G (2007) Preapoptotic chromatin changes induced by ultraviolet B irradiation in human erythroleukemia K562 cells. Apoptosis 12:2089–2099